Journal of Marine Science and Application (2021) 20:284–301
https://doi.org/10.1007/s11804-021-00211-4

RESEARCH PAPER

Modelling and Analysis of Turning Motion of a Subsurface Mapping AUV with Split-Hull Design

Vishakh S. Kumar[1] · **Prabhu Rajagopal**[1]

Received: 22 October 2020 / Accepted: 15 March 2021 / Published online: 15 July 2021

Abstract

There is much need for autonomous underwater vehicles (AUVs) for inspection and mapping purposes. Most conventional AUVs use torpedo-shaped single-rigid hull, because of which their manoeuvrability is limited. Moreover, any increase in payload results in a larger hull size and the turning diameter, limiting its operation in constrained areas. As a solution to this problem, we develop M-Hull, a subsurface mapping AUV with a modular-split hull design that provides better manoeuvrability than a conventional torpedo-shaped vehicle. At the same time, it has more agility than an unconventional bio-inspired snake-like vehicle though their designs look similar. This approach makes it a hybrid solution between conventional torpedo-shaped AUVs and unconventional bio-inspired vehicles. We focus on improving the turning diameter during the mapping operation, and hence this paper concentrates on the dynamic aspects of the 2D turning motion of the vehicle. It will provide the relationship between turning speed, thrust, and joint torque requirements for the multi-hull underwater vehicle. Different turning modes are compared to choose an optimum turning configuration, and the critical speed is calculated for the vehicle's safe operation. In the end, the modelling is verified using the experimental data. One can follow the method followed here for the 2D motion analysis of similar underwater vehicles.

Keywords Autonomous underwater vehicle · Turning diameter · Dynamic modelling · Fluid force · Joint torque

1 Introduction

There are numerous applications for underwater vehicles for inspection and survey purposes. Bathymetry of water bodies typically involves measuring temperature, conductivity, pH and radiation levels, and visual inspection of underwater structures. The significant areas of application include the offshore oil and gas industry, defence sector, maritime search and rescue, oceanographic research, underwater archaeology, and environmental monitoring of water bodies (Antonelli 2014). Before the rise of autonomous underwater vehicles (AUVs) and remotely operated vehicles (ROVs), they were carried out manually using boats or vessels. It demanded tedious work of two or more persons during the entire operation time. It cannot guarantee the measurement's reliability due to the job's lengthy nature and human fatigue errors. Also, water bodies may contain hazardous elements that can affect the health condition of the operator. AUVs are more desirable for bathymetry as it demands less human intervention due to their autonomous mode of operation. It also has higher reliability, better safety, and hence it facilitates much effective data collection compared to manual bathymetry. Various kinds of underwater vehicles available are described below.

Article Highlights
- Split-hull design increases AUV's manoeuvrability.
- Different turning modes are possible for the split-hull AUVs.
- Critical turning speed is important to consider for split-hull vehicles.
- Joint torque and thrust requirements are optimised according to the turning mode.

✉ Vishakh S. Kumar
vishakhskumar1995@gmail.com

Prabhu Rajagopal
prajagopal@iitm.ac.in

[1] Centre for Nondestructive Evaluation, Department of Mechanical Engineering, IIT Madras, Chennai 600036, Tamil Nadu, India

1.1 Conventional Underwater Robotic Vehicles

Numerous studies and innovations have been carried out in the design and capabilities of underwater vehicles. They include the kinematic (Gherairi and Ben Hamed 2017) and

dynamic analysis of underwater robots, which is used as the basic fundamental equations for analysing an underwater vehicle. Most underwater vehicles are developed mainly for inspection and mapping purposes. Some noteworthy examples include Aqua Explorer 1000 (Kato et al. 1994), which is designed to track and inspect seabed cables. It uses a wide body hull with rear thrusters for propulsion and fins for depth control. It uses acoustic signal for data communication under the water and radio signals when it reaches the surface. But it has a bulky design that limits overall manoeuvrability and total payload. Alvarez showed how an AUV could be made with the capabilities of an underwater glider using Folaga (Alvarez et al. 2009). Instead of using the conventional rotary thrusters, it uses side jet pumps for turning. It also uses a variable buoyancy system for depth adjustment. But due to the long-slender hull, it has poor manoeuvrability in constrained spaces. Also, the variable buoyancy system takes much space from the hull. Hence, it has limited payload capacity. JAMSTEC in 1998 launched a long-distance AUV named URASHIMA that can travel up to 300 km in a single stretch and is powered by a hydrogen fuel cell (Tamura et al. 2000). It is an enormous AUV with a length of 10 m. The hull is made of Titanium, and it can operate even at a depth of 3500 m. Another important AUV is Remus, one of the most popular AUVs worldwide (Prestero 2001). It also has a long single-hull form factor. It has different variants meeting various depth and range requirements (length ranging from 1.6 to 3.84 m). There have been many studies conducted based on this vehicle. Recently, the National Institute of Oceanography (NIO) developed an AUV called Maya (Madhan et al. 2006) for ocean exploration. It is a 1.8-m-long torpedo AUV with onboard sensors for water quality test and live video recording and is designed to surge even at a depth of 200 m. It is also being used for the inspection of dam walls and ocean explorations. It relies on the fins for depth adjustments and turning. Kongsberg is one of the major players in the commercially available AUV industry. Their significant collection includes Seaglider, Munin, and Hugin AUVs. They are all competent vehicles and can carry multiple sensors, including multibeam echosounder, sidescan sonar, bottom profiler, still camera, and methane sensor. They measure from 3 to 5 m in length. They all work with the help of rear rotary thrusters and control fins for manoeuvring. They can work continuously for hours without any human intervention. Some of them, such as Seaglider M6 (Eriksen et al. 2001), can operate even at a depth of 6000 m due to their thick carbon fibre hull structure.

1.2 Unconventional Underwater Robotic Vehicles

There have been many attempts to improve underwater vehicles. Many of them concentrated on improving the hull space, manoeuvrability, and reducing the cost of transport (Kelasidi and Pettersen 2015). A popular approach is the use of multiple hulls instead of one. A notable example is LARSYS, Portugal, which developed an AUV with two parallel hulls called Medusa (Abreu et al. 2016). The hulls are arranged vertically, and the bottom hull carries heavy payloads for stability, whereas the top hull carries lighter sensors and a communication system. Each hull has a diameter of 0.15 m and a length of 1.1 m and is made of acrylic. They have developed a deep-water version of the same made of aluminium as well. Another one is from Woods Hole Oceanographic Institution (WHOI) that uses a special AUV having three parallel hulls named Autonomous Benthic Explorer (German and Yoerger 2008). It is specially designed for ocean floor mapping and can operate even at a depth of 5000 m. Though parallel hull design reduced the robot's overall length to 2 m, it increased face dimensions, making it difficult to operate in small openings. They also released another AUV named Jaguar (Kunz et al. 2009), which has two vertical parallel hulls. It is designed to hover like a helicopter to capture high quality still images in the Arctic sea under the ice layers and operate up to 20 h without any interventions. It also has a built-in manipulator and is powered by rotary thrusters in different directions. Another interesting work is from Lin, who introduced an underwater robot with a different design and locomotion system (Lin 2011). It uses a spherical hull for carrying the components and water jet thrust for propulsion. The jet can also be vectored for multi-directional movements with the minimum number of jet thrusters. Though this robot has a different shape and propulsion system, it will struggle in real-world applications as the large spherical shape will make it difficult to pass through constrained spaces. The underwater robot named HRF-2 (Chen et al. 2008) has fish-inspired vertical fins for surge thrust and a piston-cylinder-based variable buoyancy system for depth adjustment. This robot also has a cylindrical torpedo hull and is 1.1 m long and 0.22 m in diameter. Though the bio-inspired propulsion system improves locomotion efficiency at lower speeds, the maximum attainable speed is limited (less than 1 m/s) for most applications. Few people worked on flexible hulls to improve manoeuvrability. It includes snake-inspired robots. E. Kelasidi has conducted studies on underwater snake robots and found that the underwater snake robots are more energy-efficient than an ROV with conventional

rotary thrusters with respect to the cost of transportation (Kelasidi and Pettersen 2015) metric and the total consumed energy. But, conventional torpedo vehicles are capable of carrying higher payload due to their long-single hull. They are also agile to surge from one point to another due to the rotary thrusters. At the same time, snake-like robots have more flexible and sleek body structure and thus have better manoeuvrability. Pal Liljeback and Oyvind Stavdahl introduced a snake robot named Mamba (Liljeback and Stavdahl 2014) in 2014. Although it was intended to be a land robot, Kelasidi experimented (Kelasidi et al. 2016) after modifying this robot by attaching two rotary thrusters in the rear side. The basic idea was to find a solution to the snake-like robot's fundamental limitation: low surge speed. The analysis showed that using thruster for surge motion and snake-like undulation for attitude control significantly improves the vehicle's capabilities. This idea was used to develop the underwater manipulator vehicle Eelume (Liljeback and Mills 2017), which has both a snake-like body and rotary thrusters. It uses modular hulls using which the entire body can act as a robotic arm to carry out inspection and maintenance of underwater structures. More details of this vehicle and comparison with our approach are given in Section 3.3. Alessandro Crespi and Yannick Morel introduced an underwater robot named Amphirobot (3rd generation) (Crespi 2006) which is inspired from eels. It uses undulatory motion to produce thrust and navigate. They have claimed that it can surge up to the speed of human swimming. But the payload capacity of this robot is pretty limited considering its dimension. Zuo and Zhifeng introduced an amphibious snake-like robot (Zuo and Wang 2008) having serpentine motion. They have also analysed both kinematic and dynamic characteristics of the same. They tried to optimise the amplitude and frequency of undulation to maximise the speed of motion. But they could barely touch 0.1 m/s, which is pretty low for real-world applications.

2 Motivation for Developing an Improved AUV

There was a need to map the physical parameters of a lake used for dumping the coolant water of a nuclear reactor. The parameters to be mapped include temperature, pH level, radiation level, and available depth at various lake locations. This data is essential for studying environmental impacts due to the operation of the nuclear reactor. AUVs are more suitable for this task as they can operate, collect, and produce a map of the entire water body's physical parameters without any human intervention for hours. This reduces risk to the human operator as the water body may contain harmful contents, especially in the case of nuclear reactors. But, we encountered some issues with the conventional AUV design during the operation plan. As mentioned in Section 1.1, the long, rigid, and bulky hull can cause difficulty in manoeuvring and controlling the vehicle. For example, the length of a standard Munin AUV is 3.5 m, indicating that at least 3.5-m width is required for a proper U-turn operation. This makes it difficult to operate the vehicle when space is restricted. The lake where we need to operate contains many areas where the width is less than 1 m. This makes it challenging to produce a map of the entire lake with such a vehicle. Also, most lakes have narrow and constrained spaces in the bed area. Since the vehicle has to be designed for more versatile operations, the scenario of heaving into the lake bed has to be considered. In that case, operating the vehicle with a large turning diameter is highly undesirable. Another issue with high turning diameter is associated with the data resolution of the map. During the operation, the vehicle has to travel along straight parallel paths all over the water body to produce the data map. U-turn with lower turning diameter facilitates lower distance between the parallel paths and provides a higher resolution of the data map. Hence, a smaller turning diameter is significant for the mapping operation in constrained areas and good data resolution. But in conventional AUVs, higher turning diameter limits its operation in constrained areas and requires additional motion controls to increase the mapping resolution. These issues inspire the idea of splitting the hull, and it is shown in Figure 1, where the total length of the vehicle is l. Splitting the hull increase the overall flexibility of the vehicle and decreases the turning diameter. More details about the design and work are explained in the next section.

This paper is organised as follows. First, the design aspects of the vehicle and novelty details are explained. This is followed by a dynamic analysis of the vehicle in turning motion, including the calculation of thrust and joint torque requirements for turning. Also, different turning modes are

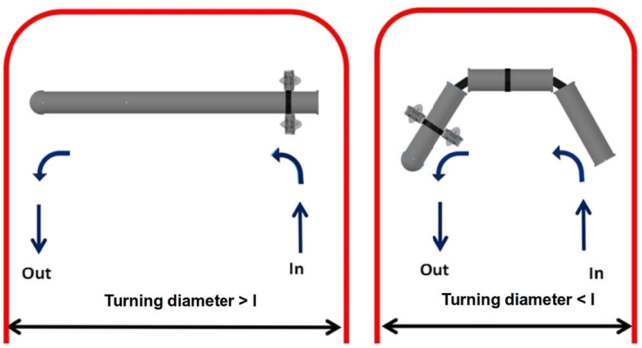

Figure 1 Schematic diagram comparing the space requirement during a U-turn for a single-hull AUV and a split-hull AUV with same dimensions

compared, and the critical turning speed is calculated. These results are verified experimentally in the end.

3 Details of Proposed Novel M-Hull AUV

3.1 Design and Working

Based on the split-hull concept, the vehicle is designed with three hulls in series. The name M-Hull is inspired by its multi-hull design. The snapshot of CAD modelling is shown in Figure 2a. Each hull is 0.426 m (With connecting link) in length and 0.1 m in diameter. The dimensions are chosen based on the payload requirements and the operating space constraint to have a turning diameter of less than 1 m. Each hull's inside length must be at least 0.34 m to carry the electronic module and the battery. Then, the diameter is chosen based on the slender body criteria, which is discussed in Section 4.4. The leading front hull carries the sensors and surge thrusters, and the middle hull carries the onboard computer and heave thrusters. The rear hull carries batteries powering the entire vehicle. We have considered the use of an undulatory/oscillatory locomotion system as in the case of snake/fish inspired robots (Wiens and Nahon 2012; Wang et al. 2017). Although it has better manoeuvrability than conventional AUVs, agility is very low (Rollinson 2014), which is essential for bathymetry. The operation must be carried out with minimum time for which higher surge speed (Punning and Anton 2004) is essential. Hence, we chose rotary thrusters for locomotion because of which the length of each hull has no direct influence on the efficiency compared to a bio-inspired (Yu and Wang 2007) locomotion system. This allowed us to design the hulls with equal length making the vehicle almost symmetric about the middle hull (Kumar and Rajagopal 2019). The vehicle can be turned either by turning the hulls using servo joints or using the differential speed of surge thrusters. But the servo method is preferred as it offers better control on yaw motion. The vehicle has independent control over Surge, Yaw, and Heave movements. The vehicle is fabricated based on this design, and it is shown in Figure 2b. The technical specifications of the vehicle are shown in Table 1. The central computer in the middle hull has a communication device, and it also stores the sensor data during the mapping operation. The sensors attached to the vehicle include a camera, temperature-pressure sensor, GPS module, and an altimeter. Once the mapping/bathymetry operation is completed, the sensor readings are fused to produce the 2D map of the water body for a particular depth.

Table 1 Technical specifications of M-Hull

Mass of the vehicle (m_t)	11.23 kg
Material	Delrin, acrylic, aluminium
Total length	1.28 m
Hull outer diameter	0.10 m
Maximum surge thrust	48 N
Maximum joint torque	1.14 N·m
Designed surge speed	1 m/s
Depth rating	10 m
Battery life (for 1 m/s)	6 hrs

3.2 Details About Joint Control for Turning

When we fabricated the vehicle, the initial plan was to use the surge thrusters for the differential drive on the front hull to obtain turning motion. Turning the robot in that way

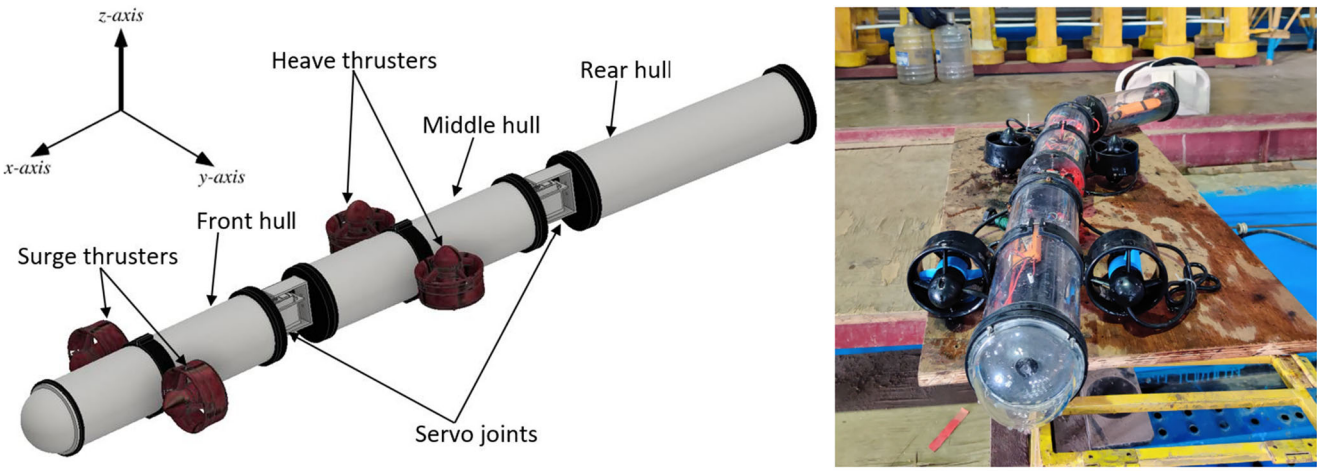

(a) Conceptual design of M-Hull (b) Photograph of M-Hull

Figure 2 Conceptual design and fabricated form of M-Hull AUV showing important parts

would get the job done. But we encountered some issues while operating the robot in water. The major one was the drift/slipping of the hulls. When the robot was following a straight-line path, there were no issues. As long as the surge thrusters can provide sufficient thrust to counteract the hydrodynamic drag forces (Venugopal et al. 2009), the front hull will move, and the other two hulls will follow it with the same velocity. But while taking turns, the situation becomes complex as the following hulls get dragged away from the path instead of following the front hull's path. This is because the robot is operating in a fluid and unlike a land-based differential drive wheeled robot, chances for slipping are very high. In the land robot, the high friction at the point of contact between wheels and the surface prevents it from slipping. But the relatively poor contact force between the fluid and robot body cannot hold the hulls on the path. When sliding occurs, the hull's cylindrical face is no longer parallel to the relative water flow and gets directly exposed to the water motion in the perpendicular direction. Hence, it is acted (Antonelli et al. 2016) by heavy normal fluid forces and the tangential forces. This increases the energy requirements of the vehicle (Kelasidi and Pettersen 2015). Thus, we used a servo-based joint controller for taking turning motion which ensures that hulls are fixed to a particular orientation while taking a turn. This also facilitates better control over turning angle and reduces the chances for hull slipping.

3.3 Novelty and Comparison with Existing Solutions

3.3.1 With Conventional Torpedo-Shaped Vehicles

M-Hull is derived as an enhanced version of conventional torpedo-shaped vehicles. The split-hull design provides much better manoeuvrability than the conventional design, as mentioned in Section 2. This makes it ideal for long-term mapping operations where data resolution is essential and where the operating region is constrained.

3.3.2 With Normal Snake-Like Vehicles

It is interesting to note that the proposed design has some similarities with normal snake-like vehicles. But they are entirely different in terms of their locomotion systems. M-Hull uses rotary thrusters like a torpedo-shaped vehicle for surge/heave motion. In contrast, a regular snake-like vehicle uses body movements such as lateral undulation/oscillation (Sverdrup-Thygeson and Kelasidi 2018). The use of thrusters makes M-Hull highly agile and allows it to operate at much higher speeds (even 2 m/s) compared to a snake-like vehicle that has less than 0.5 m/s (Liljeback and Stavdahl 2014; Crespi 2006) average operating speed. This is very useful as it reduces overall operation time. M-Hull uses body movements only for changing its orientation or for yaw motions with servo-controlled joints.

3.3.3 With Snake-Like Vehicles Having Thrusters

It is worth mentioning about Eelume, which is a flexible, snake-like vehicle propelled by conventional thrusters (Liljeback and Mills 2017). It is designed for a different purpose as an underwater swimming manipulator and carry out the intervention in confined spaces as an ROV. But M-Hull is an independently developed AUV that is specifically designed for mapping water bodies. A vehicle that can map the entire water body by operating in particular depth with minimum energy expenditure is ideal for such a task. M-Hull is equipped with neutrally buoyant hulls and single-axis connecting links to prevent unwanted pitch movements without spending any energy. Eelume has double-axis joints that facilitate pitch and yaw motions required for manipulator tasks. But this feature is undesirable for mapping water bodies for bathymetry as it demands continuous power for the pitch controller. This is not desirable for more extended operations as the pitch controller will consume a significant amount of energy in addition to the thrusters. Thus, M-Hull can perform the automated bathymetry operations more efficiently compared to existing solutions as it is specifically designed for that purpose.

In addition to the novelty in the design and working of this vehicle, to the author's best knowledge, detailed modelling, analysis, and experimental verification of the turning motion of a split/multi-hull underwater vehicle with rotary thrusters have not been considered in previous literature. The results of this work will be beneficial to the development of similar underwater vehicles. Further details about the turning analysis are explained in the next section.

4 Modelling the Turning Motion

The basic idea of split-hull design is to enhance the turning and manoeuvring capabilities of underwater vehicles. It is essential to find out the merits and demerits of having this design over the conventional approach. Thus, detailed modelling and analysis are carried out on M-Hull's turning motion, which will help control system design later. Let us consider the case when the vehicle is tracing a circular path. As the servo-controlled joint can hold the hulls at a particular angular position, each hull's orientation can be maintained accurately during the turn. This makes the vehicle look like a part of a polygon, and the path acts as its inscribed circle. This is shown in Figure 3a. For this analysis, we assume that the entire motion takes place only in the XY plane and the rolling/pitching motions are absent.

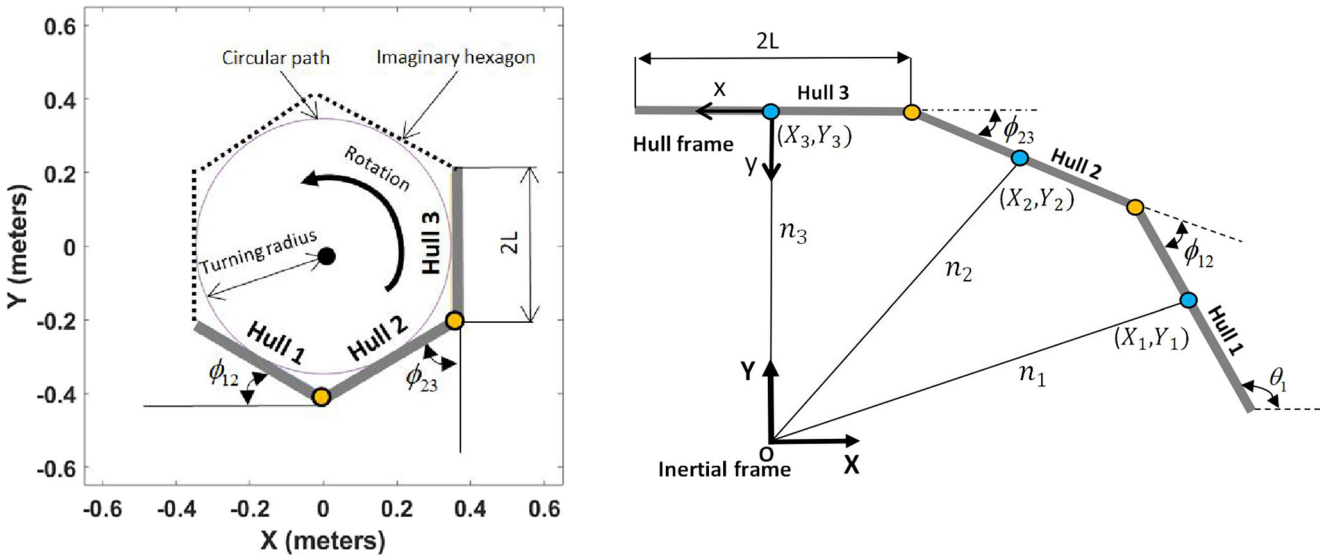

(a) Hexagonal configuration during U-turn (b) Kinematic parameters of the vehicle

Figure 3 Schematic diagram showing the hexagonal configuration and kinematic parameters while taking a U-turn

The fluid considered here is viscous, static, incompressible, and irrotational (Jagadeesh et al. 2009). The turning path considered is perfectly circular with no hull slipping. The kinematic modelling is explained below.

4.1 Kinematic Modelling

To understand this multi-body system's behaviour during the turning motion, we need to conduct a detailed analysis. Note that the entire mapping operation occurs in a 2D plane (XY), and hence heave (Z) motions are ignored here. The schematic diagram of the kinematic parameters for turning motion is shown in Figure 3b. The notations used for the parameters are given in Table 2. The inertial frame XY is fixed at the centre of the circle, and we follow the inverse kinematic approach. The vehicle is made to trace a circular path for a certain time at a fixed angular speed (ω). The corresponding parameters such as velocity, acceleration, joint force, joint torque, and thrust requirement are calculated. Table 3 provides all the parameters to be calculated. The basic kinematic constraint equations are given in Eqs. (1)–(4). There are nine kinematic constraint equations ($C_1 - C_9$) where R is the radius of curvature of the path, and β is the turning angle used for the simulation. This is solved for finding out the position vector (X_i, Y_i, θ_i) for all the hulls corresponding to the angular position of the vehicle (β) while tracing the circular path. Note that $\boldsymbol{T}_i$ is the coordinate transformation matrix from ith hull frame to the inertial frame.

$$\begin{bmatrix} C_1 \\ C_2 \end{bmatrix} = \begin{bmatrix} X_3 \\ Y_3 \end{bmatrix} - \begin{bmatrix} R\cos(\beta) \\ R\sin(\beta) \end{bmatrix} = 0 \quad (1)$$

$$\begin{bmatrix} C_3 \\ C_4 \end{bmatrix} = \begin{bmatrix} X_1 \\ Y_1 \end{bmatrix} + \boldsymbol{T}_1 \begin{bmatrix} L \\ 0 \end{bmatrix} - \begin{bmatrix} X_2 \\ Y_2 \end{bmatrix} - \boldsymbol{T}_2 \begin{bmatrix} -L \\ 0 \end{bmatrix} = 0 \quad (2)$$

$$\begin{bmatrix} C_5 \\ C_6 \end{bmatrix} = \begin{bmatrix} X_3 \\ Y_3 \end{bmatrix} + \boldsymbol{T}_3 \begin{bmatrix} -L \\ 0 \end{bmatrix} - \begin{bmatrix} X_2 \\ Y_2 \end{bmatrix} - \boldsymbol{T}_2 \begin{bmatrix} L \\ 0 \end{bmatrix} = 0 \quad (3)$$

Table 2 List of parameters used for the dynamic analysis

Symbol	Meaning
θ_i	Orientation of hull i with X axis (rad)
ϕ_{ij}	Joint angle between hull i and j (rad)
m_i	Mass of hull i (kg)
I_i	Moment of inertia of hull i about z axis (kg·m^2)
$2L$	Length of each hull = 0.426 m
D	Diameter of each hull ($2r$) = 0.1 m
R	Radius of curvature of path (m)
ρ	Density of water (1000 kg/m^3)
β	Turning angle (rad)
ω	Angular velocity of turning (rad/s)

Table 3 List of all parameters to be calculated from the dynamic analysis

T_X	Surge thrust X component (N)
T_Y	Surge thrust Y component (N)
h_{Xij}	Joint force in X direction between hull i and j (N)
h_{Yij}	Joint force in Y direction between hull i and j (N)
τ_{ij}	Joint torque between hull i and j (N·m)

$$\begin{bmatrix} C_7 \\ C_8 \\ C_9 \end{bmatrix} = \begin{bmatrix} \theta_3 - \pi/2 - \beta \\ \theta_2 - \theta_1 - \phi_{12} \\ \theta_3 - \theta_2 - \phi_{23} \end{bmatrix} = 0 \tag{4}$$

$$\boldsymbol{T}_i = \begin{bmatrix} \cos(\theta_i) & -\sin(\theta_i) \\ \sin(\theta_i) & \cos(\theta_i) \end{bmatrix} \tag{5}$$

The constraint equations $C_1 - C_9$ can be written in short as $\boldsymbol{C} = 0$ and solving it will give the global position vector $\boldsymbol{X}_t \in V^{9\times1}$ for any turning angle β. First and second time derivatives of $\boldsymbol{C}$ are given as

$$\frac{\partial \boldsymbol{C}}{\partial t} = \frac{\partial \boldsymbol{C}}{\partial \boldsymbol{X}_t}\dot{\boldsymbol{X}}_t = J\dot{\boldsymbol{X}}_t = 0 \tag{6}$$

$$\frac{\partial^2 \boldsymbol{C}}{\partial t^2} = \frac{\partial \boldsymbol{J}}{\partial \boldsymbol{X}_t}\dot{\boldsymbol{X}}_t{}^2 + \boldsymbol{J}\ddot{\boldsymbol{X}}_t = 0 \tag{7}$$

$$\boldsymbol{X}_t = [X_1\ Y_1\ \theta_1\ X_2\ Y_2\ \theta_2\ X_3\ Y_3\ \theta_3]^{\mathrm{T}} \tag{8}$$

where $\boldsymbol{J}$ is the Jacobian matrix of the constraint equations which will be calculated in the next section. Substituting $\dot{\beta} = \omega$ in the Eq. (6) will provide the values of the velocity matrix $\dot{\boldsymbol{X}}_t$ at any turning angle β. Using this and then by substituting $\ddot{\beta} = 0$ in the Eq. (7) will give the values of the corresponding acceleration matrix $\ddot{\boldsymbol{X}}_t$. This is the algorithm used in the simulation to find out the kinematic parameters for each hull.

4.2 Dynamic Modelling

The split-hull design of the vehicle makes it possible to analyse the dynamics of each hull separately. Note that the rear hull is numbered as one, and the front one is numbered as three. The mass of each hull is given as $m_1 = 3.35$ kg and $m_2 = m_3 = 3.94$ kg. Let us calculate the moment of inertia (I_i) about the z-axis. The hulls are considered as cylinders of diameter 0.1 m and length 0.426 m. The servo joint between each hull is taken as an extension of each hull. Since the front and middle hulls are having thrusters attached, their contributions have to be included. One more point to be noted is the difference in orientation of the thrusters. Front hull thrusters face the surge direction, but the middle hull thrusters face the heave direction. The calculation is as follows. Moment of inertia about the z-axis for each hull (Without thrusters) with mass m_1 and length $2L$ is given by $I_0 = m_1\frac{(2L)^2}{12} = 0.0506\ \mathrm{kg}\cdot\mathrm{m}^2$. Each thruster is considered as a hollow cylinder of mass m_t= 0.295 kg with outer radius r_o= 0.05 m and inner radius r_i= 0.038 m. The offset of each thruster from the axis of the cylinder is l_{off}= 0.11 m. The parallel axis theorem gives the following values. As the rear hull has no thrusters attached, only the contribution of the hull will be used. Hence,

$$I_1 = I_0 = 0.0506\ \mathrm{kg}\cdot\mathrm{m}^2 \tag{9}$$

$$I_2 = I_0 + m_t(r_0^2 + r_i^2 + 2l_{\mathrm{off}}^2) = 0.0583\ \mathrm{kg}\cdot\mathrm{m}^2 \tag{10}$$

$$I_3 = I_0 + \frac{m_t}{6}(3(r_0^2 + r_i^2) + h^2 + 12l_{\mathrm{off}}^2) = 0.0578\ \mathrm{kg}\cdot\mathrm{m}^2 \tag{11}$$

Dynamic modelling of M-Hull is a multi-body analysis. We follow the modified form of the augmented equation formulation method or open-chain method (Betsch 2018), which is generally used for the dynamic analysis of open-chain mechanisms. This method is valid for link mechanisms with one end open and the other end pivoted (Shabana 2013). M-Hull has both ends open, and hence it has to be modified. It states the multi-body dynamic equation as the summation of two force components $\boldsymbol{F}_e$ and $\boldsymbol{F}_c$.

$$\boldsymbol{M}\ddot{\boldsymbol{X}}_t = \boldsymbol{F}_e + \boldsymbol{F}_c \in V^{9\times1} \tag{12}$$

$$\boldsymbol{M} = diag[m_1, m_1, I_1, m_2, m_2, I_2, m_3, m_3, I_3] \in V^{9\times9} \tag{13}$$

where $\boldsymbol{M}$ is the mass-inertia matrix and $\boldsymbol{X}_t$ is the global position vector given in Eq. (8). Note that this method uses values expressed in the global/inertial frame. $\boldsymbol{F}_e \in V^{9\times1}$ is the fluid external force matrix that includes net external force in X direction (F_{iX}), Y direction (F_{iY}), and concentrated external torque (τ_i) on each hull. They are shown in Figure 4 and are calculated in Section 4.4.

$$\boldsymbol{F}_e = \left[\ F_{1X}\ F_{1Y}\ \tau_1\ F_{2X}\ F_{2Y}\ \tau_2\ F_{3X}\ F_{3Y}\ \tau_3\ \right]^{\mathrm{T}} \tag{14}$$

The second term, $\boldsymbol{F}_c \in V^{9\times1}$ is the modified form of constraint force matrix ($\boldsymbol{H}$) given by $\boldsymbol{F}_c = \boldsymbol{J}^{\mathrm{T}}\boldsymbol{H}$. This includes all the internal joint forces (h_{Xij}, h_{Yij}) and joint torques (τ_{ij}). Usage of the Jacobian ($\boldsymbol{J}$) makes it possible

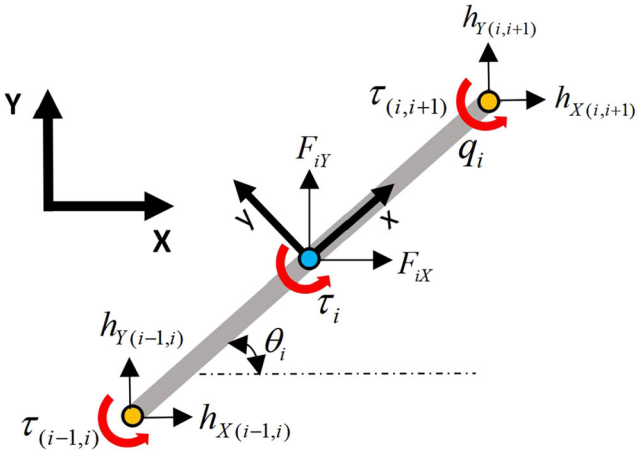

Figure 4 Schematic diagram showing the forces and torques acting on the hull

to include these internal forces in the overall multi-body dynamic equation as given below.

$$\boldsymbol{F}_c = \boldsymbol{J}^{\mathrm{T}} \left[h_{X30}\ h_{Y30}\ h_{X12}\ h_{Y12}\ h_{X23}\ h_{Y23}\ \tau_{30}\ \tau_{12}\ \tau_{23} \right]^{\mathrm{T}} \tag{15}$$

Note that $\boldsymbol{H}$ includes the total thruster force required for the vehicle given by $[h_{X30}\ h_{Y30}]^{\mathrm{T}}$, which is an internal force with respect to the vehicle. This results in both axial and lateral thrust requirements when transformed into hull coordinates. But the lateral component is negligible for the polygonal turning modes we consider for the analysis as the individual hull forces cancel out. Adding this to the fact that we do not use sway thrusters, we ignore the lateral thrust component in this paper. The absence of lateral thrust will result in vehicle slipping, which we will discuss in the experimental results. The axial thrust force requirement (T) is obtained by transforming it into hull coordinate as

$$T = C_3 h_{X30} + S_3 h_{Y30} \tag{16}$$

We use the terms S_i=sin(θ_i), C_i=cos(θ_i), S_β=sin(β) and C_β=cos(β). Note that we consider $\boldsymbol{F}_c$ in such a way that it acts as the driving force that handles the external disturbance ($\boldsymbol{F}_e$) and results in the dynamics of the vehicle as $\boldsymbol{M}\ddot{\boldsymbol{X}}_t$. Jacobian matrix is obtained from the constraint equations ($\boldsymbol{C}_i$) given in Eqs. (1)–(4) and is calculated as $\boldsymbol{J} = \partial \boldsymbol{C}_i / \partial \boldsymbol{X}_{tj},\ i, j \in [1, 9]$ from which its transpose is given by

$$\boldsymbol{J}^{\mathrm{T}} = \begin{bmatrix} 0 & 0 & 1 & 0 & 0 & 0 & 0 & 0 & 0 \\ 0 & 0 & 0 & 1 & 0 & 0 & 0 & 0 & 0 \\ 0 & 0 & -LS_1 & LC_1 & 0 & 0 & 0 & -1 & 0 \\ 0 & 0 & -1 & 0 & -1 & 0 & 0 & 0 & 0 \\ 0 & 0 & 0 & -1 & 0 & -1 & 0 & 0 & 0 \\ 0 & 0 & -LS_2 & LC_2 & LS_2 & -LC_2 & 0 & 1 & -1 \\ 1 & 0 & 0 & 0 & 1 & 0 & 0 & 0 & 0 \\ 0 & 1 & 0 & 0 & 0 & 1 & 0 & 0 & 0 \\ RS_\beta & -RC_\beta & 0 & 0 & LS_3 & -LC_3 & 1 & 0 & 1 \end{bmatrix} \in V^{9\times 9} \tag{17}$$

The value of thrust T is significant as it indicates whether the thruster is capable of providing enough thrust for achieving the desired turning motion or not. Joint forces such as h_{X12}, h_{Y12}, h_{X23}, and h_{Y23} are important for the design of the connecting link mechanism. The joint torques τ_{12} and τ_{23} are required for the selection of servo motor and are critical parameters during the turning motion details about which is given in Section 5. Note that the constraining force matrix ($\boldsymbol{H}$) can be obtained using these values as

$$\boldsymbol{H} = (\boldsymbol{J}^{\mathrm{T}})^{-1}(\boldsymbol{M}\ddot{\boldsymbol{X}}_t - \boldsymbol{F}_e) \in V^{9\times 1} \tag{18}$$

The acceleration matrix $\ddot{\boldsymbol{X}}_t$ is calculated as explained in the kinematic modelling, and the external force matrix $\boldsymbol{F}_e$ is calculated using the method discussed in Section 4.4. Equation 18 is solved during each instant of the turning motion (by varying β value), and all the corresponding parameters are calculated. But there is a crucial point to be noted before proceeding further, and it is discussed below.

4.3 Modification in the Open-Chain Method

Although $\boldsymbol{H}$ gives all the required parameters given in Table 3, we do not completely depend on Eq. (18) as M-Hull has both ends open and the open-chain method's validity has to be verified in our case. Suppose we expand (12) by substituting the external force matrix given in Eq. (14) and the Jacobian values given in Eq. (17). In that case, we will get the following dynamic (19)–(27) for each hull (Given with respect to the respective centre of buoyancy). We also showed the corresponding dynamic force-torque diagrams in Figure 5a–c for better understanding. Let us examine the dynamic equations for each hull. Note that these balance equations and figures are based on the open-chain method and hence will have to be modified for M-Hull in the next step.

4.3.1 Hull 1

The dynamic balance diagram is shown in Figure 5a and the corresponding equations are

$$F_{1X} + h_{X12} = m_1 \ddot{X}_1 \tag{19}$$

$$F_{1Y} + h_{Y12} = m_1 \ddot{Y}_1 \tag{20}$$

$$-\tau_{12} + \tau_1 - L\sin(\theta_1) h_{X12} + L\cos(\theta_1) h_{Y12} = I_1 \ddot{\theta}_1 \tag{21}$$

4.3.2 Hull 2

The dynamic balance diagram is shown in Figure 5b and the corresponding equations are

$$F_{2X} - h_{X12} - h_{X23} = m_2 \ddot{X}_2 \tag{22}$$

$$F_{2Y} - h_{Y12} - h_{Y23} = m_2 \ddot{Y}_2 \tag{23}$$

$$\begin{aligned} &\tau_{12} - \tau_{23} + \tau_2 - L\sin(\theta_2) h_{X12} + L\cos(\theta_2) h_{Y12} \\ &+ L\sin(\theta_2) h_{X23} - L\cos(\theta_2) h_{Y23} = I_2 \ddot{\theta}_2 \end{aligned} \tag{24}$$

4.3.3 Hull 3

The dynamic balance diagram is shown in Figure 5c and the corresponding equations are

$$F_{3X} + h_{X23} + T_X = m_3 \ddot{X}_3 \tag{25}$$

$$F_{3Y} + h_{Y23} + T_Y = m_3 \ddot{Y}_3 \tag{26}$$

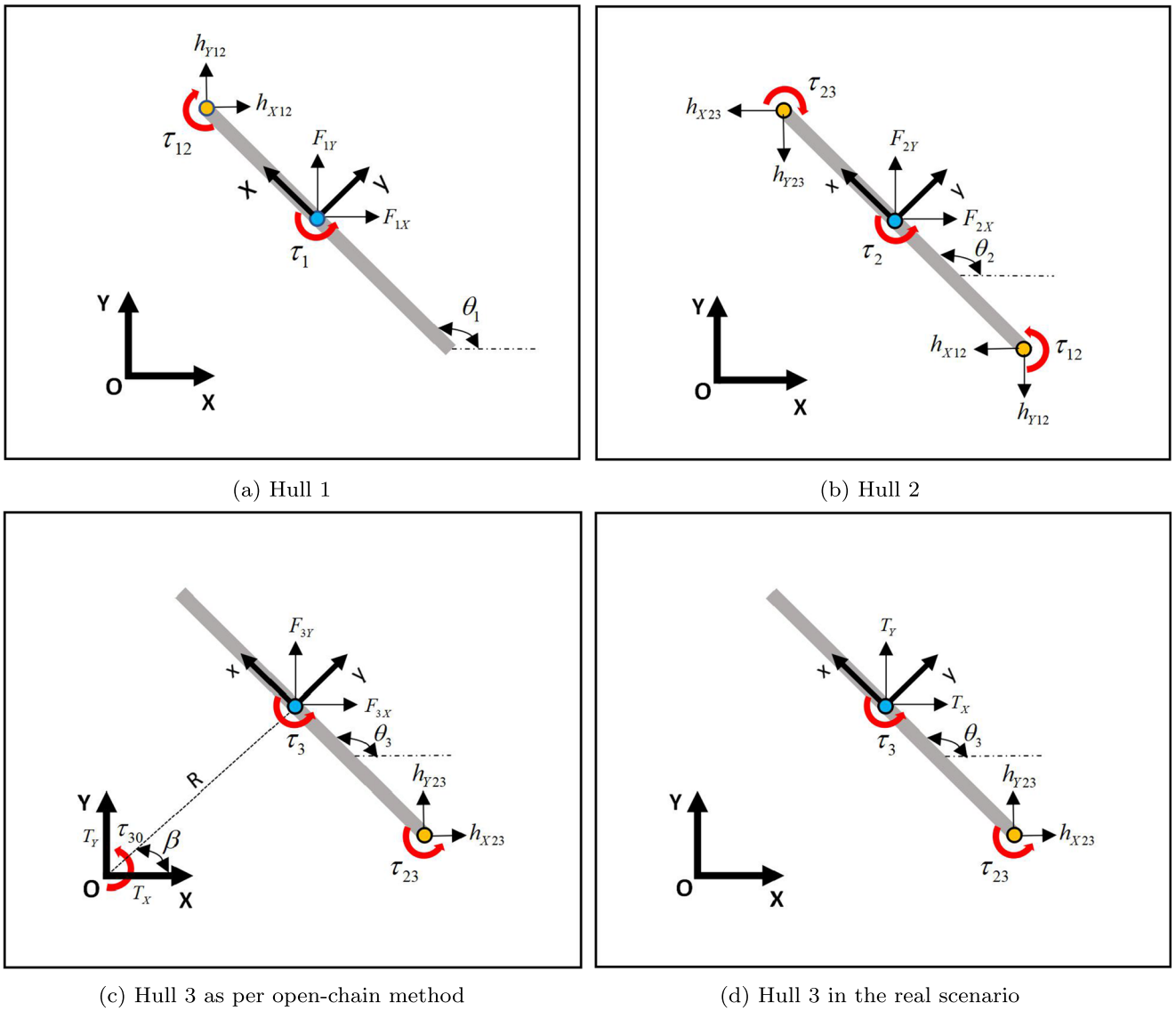

(a) Hull 1 (b) Hull 2

(c) Hull 3 as per open-chain method (d) Hull 3 in the real scenario

Figure 5 Schematic diagram showing the Forces and torques acting as per open-chain method

$$\tau_{23} + \tau_{30} + L\sin(\theta_3)h_{X23} - L\cos(\theta_3)h_{Y23} + R\sin(\beta)T_X - R\cos(\beta)T_Y = I_3\ddot{\theta}_3 \quad (27)$$

Analysing (19), (20), (22), (23), (25), and (26), one can verify that they all are general force balance equations and hence are valid in our case. But there is an issue in the case of torque balance (21), (24), and (27). This is because the open-chain method assumes that the third hull is pivoted to the inertial reference centre, as shown in Figure 5c, and hence it is not the correct representation of the forces/torques on hull 3. The real force-torque diagram for hull three is shown in Figure 5d, and that for hull 1 and 2 are the same as Figure 5a and b, respectively. The issue with the open-chain method on the torque is described as follows. The torque requirements on hull two and hull 1 add up to the torque requirement on hull 3 (τ_{30}), which is clear from Eq. (27). This is valid for an open-chain mechanism where one link is pivoted to the reference point, but there is no such pivot point for an underwater vehicle, and τ_{30} becomes a non-existing torque. Thus, some modifications are required for the proper calculation of the torque. We carry out additional analysis, as shown below. The joint torque is required to balance out two components: One due to the external normal force (f_{iy}) on the hull, which is explained in the next section and the other due to the centrifugal force ($m_i R\omega^2$) of each hull. The action of these forces to push the hulls outwards and the counteraction by joint torques (τ_{ij}) to maintain the vehicle orientation are shown in Figure 6. As there are three hulls with two joints, we assume that each joint's total torque acting is equally handled. The first joint will handle the net torque on the first hull and half of the second hull. Similarly, the second

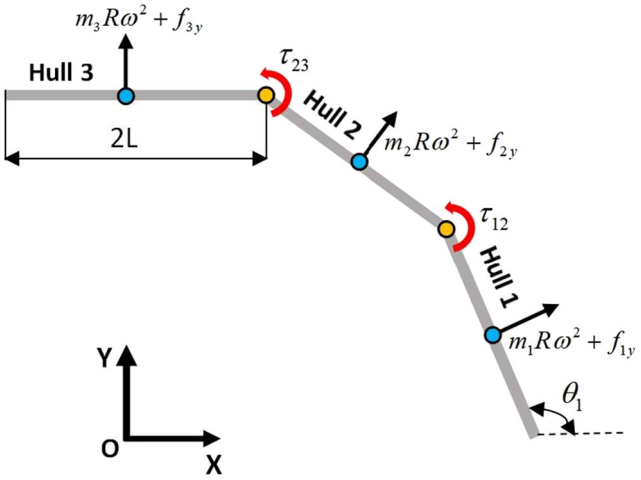

Figure 6 Schematic diagram showing forces that cause bending moment on the joints

joint will handle the torque on the third hull and half of the second hull. Hence, the torque requirement for each joint is given as

$$\tau_{12} = \left(\frac{2f_{1y} + f_{2y} + (2m_1 + m_2)R\omega^2}{2}\right) L \tag{28}$$

$$\tau_{23} = \left(\frac{2f_{3y} + f_{2y} + (2m_3 + m_2)R\omega^2}{2}\right) L \tag{29}$$

It is important to note that the thrust requirement is calculated from Eqs. (16) and (18). The modification from the open-chain method does not affect the validity of force balance equations. The drag and added mass forces are calculated in the hydrodynamic modelling discussed in the next section.

4.4 Calculation of External Fluid Force Matrix: F_e

We model the external fluid forces while considering all the hydrodynamic effects significant for the vehicle control system. We follow Morison's equation (Morison et al. 1950) for the fluid force calculation as each hull is a slender cylinder (Cox 1970) with a length more than four times the diameter (0.42 m vs 0.10 m). Also, note that the external concentrated fluid torque (τ_i) on each hull given in Eq. (14) is zero, and the torque action due to the fluid force moment is calculated in Section 4.3. The total external force on the hull i is calculated as the sum of added mass force ($\boldsymbol{F}_{Ai}$) and drag force ($\boldsymbol{F}_{Di}$) and is given by

$$\boldsymbol{F}_{ei} = \boldsymbol{F}_{Ai} + \boldsymbol{F}_{Di} \in V^{2\times 1} \tag{30}$$

where added mass force for ith hull ($\boldsymbol{F}_{Ai}$) is obtained by transforming added mass force in the hull coordinates $\boldsymbol{f_{Ai}}$ into inertial coordinates as in Eq. (31) where C_{Ai} is the added mass coefficient matrix and is given below. $\dot{\boldsymbol{v}}_{ri}$ is the relative acceleration vector of fluid defined along the hull frame, and it is given below.

$$\boldsymbol{F}_{Ai} = \boldsymbol{T}_i \boldsymbol{f}_{Ai} = \boldsymbol{T}_i \boldsymbol{C}_{Ai} \dot{\boldsymbol{v}}_{ri} \in V^{2\times 1} \tag{31}$$

$$\dot{\boldsymbol{v}}_{ri} = -\begin{bmatrix} \dot{v}_{xi} & \dot{v}_{yi} \end{bmatrix}^{\mathrm{T}} \qquad \boldsymbol{C}_{Ai} = \begin{bmatrix} 0 & 0 \\ 0 & \frac{1}{4}\rho\pi C_a D^2 L_e \end{bmatrix} \tag{32}$$

L_e is the effective length given to each hull, including the thruster effect. It is equal to $2L$ for rear hull, $2L + 2L_t$ for middle hull and $2L + 2h_t$ for front hull. $h_t = 0.056$ m is the height and $L_t = 0.1$ m is the length of thruster. As the vehicle is turning at a constant speed, $\dot{v}_{xi} = 0$. But $\dot{v}_{yi} = R\omega^2$ due to the centripetal acceleration, and it results in the added mass force in the y-direction. This added mass component is the speciality of rotational motion as it acts even though it has zero tangential acceleration. This is interesting, and it is also known as centripetal acceleration reaction force (Zhang et al. 2015). C_a is the lateral drag coefficient, and it depends on the working conditions, including the type of flow, size, and shape of the body and it is given in the next section. Note that the added mass force in the x-direction is negligible because the axial added mass is very less compared to the body mass for a slender cylinder (Newman and Grue 1977)). Note that individual hulls are symmetric about all the principal planes. Hence, we omit all the cross added mass terms in this analysis. The drag force $\boldsymbol{F}_{Di}$ is given below, where we have taken it as a function of both first and second orders of velocity and $\boldsymbol{C}_{Di}$ is the drag coefficient matrix.

$$\boldsymbol{F}_{Di} = \boldsymbol{T}_i \boldsymbol{f}_{Di} = \boldsymbol{T}_i (\boldsymbol{C}_{Di} \boldsymbol{v}_{ri} + \boldsymbol{C}_{Di} \boldsymbol{v}_{ri} |\boldsymbol{v}_{ri}|) \in V^{2\times 1} \tag{33}$$

$$\boldsymbol{C}_{Di} = \begin{bmatrix} \frac{1}{4}\rho\pi C_f D L_e & 0 \\ 0 & \frac{1}{2}\rho C_d D L_e \end{bmatrix} \tag{34}$$

Note that $\boldsymbol{v}_{ri}$ is the relative velocity of the fluid with respect to each hull in the hull frame. As we consider static water, the relative velocity is equal to the negative of the vehicle velocity and C_f is the drag coefficient along x direction and C_d is the drag coefficient along y direction. The relative velocity vector in i^{th} hull frame is given by

$$\boldsymbol{v}_{ri} = -\begin{bmatrix} v_{xi} & v_{yi} \end{bmatrix}^{\mathrm{T}} \tag{35}$$

As the hull is assumed to be having no sliding in the sway direction, v_{yi} is zero for all hulls. Now let us choose the hydrodynamic coefficients. They are chosen based on the steady-state flow condition. Many experiments have been conducted on cylinders in steady-state flow under conditions similar to M-Hull (Gus'kova et al. 1998; Kelasidi 2015; Khalil and Gallot 2007). With an operating speed of 0.4 m/s and considering Reynolds number in the range of 10^5 (Transition region) (Wiens and Nahon 2012), the coefficients for a uniform smooth cylinder can be taken as (Kelasidi 2015) $C_d = 1$, $C_a = 1$, and $C_f = 0.03$ (for straight motion). But in our case, there will be additional

drag effects due to non-cylindrical link joints, external wires, and thrusters. We estimated this effect using CFD analysis and found that the drag effect is 1.6 times that of a smooth cylinder of the same dimensions. Hence, we selected the drag coefficients as C_d = 1.65, C_f = 0.048, and C_a = 1. Let us use these values in the dynamic analysis of the vehicle. All the parameters to be calculated from the dynamic analysis are shown in Table 3.

4.5 Selection of the Turning Mode (n)

Before experimenting to verify this dynamic modelling's validity, it is important to select the turning mode discussed in the following section. The vehicle can be configured in different ways using the servo joints between hulls. The servo joints can rotate up to 90° on both sides. If the required torque is within the range of servo, the rotation angle can be precisely controlled. The servo can provide up to 1.14 N·m torque. The analysis is carried out to compare different configurations of the vehicle while turning. The only difference between each configuration is the relative orientation of each hull (ϕ_{ij}). We define a new parameter called turning mode number (n). The configurations are shown below in Figure 7a–d. We chose the turning angles as 72° for pentagonal configuration ($n = 5$), 60° for hexagonal configuration ($n = 6$), 51.4° for heptagonal configuration ($n = 7$), and 45° for octagonal configuration ($n = 8$). Since there are three hulls for the vehicle, choosing n below 4 (rectangular configuration) is not a good idea. For example, if $n = 3$, the hulls will orient as a part of a triangle and collide. Also, this will demand too much effort from the servo motors, which will be discussed in the coming section. Hence, for the experimental study, turning modes from pentagonal ($n > 4$) are chosen. The increase in turning diameter in each case is visible from the same figures.

4.6 Simulation Methodology

The analysis is carried out assuming that path of each hull is in a perfect circular shape. So, the orientation of each hull with respect to the other one has to be kept constant. This requires sufficient torque from the servo in each joint. Though the design speed is 1 m/s, a lower turning speed is taken for safety. The kinematic parameters are calculated using Eqs. (6) and (7) for 0.4 m/s, turning speed for one revolution along a circular path. Hence, the rotation angle of β will change from 0 to 2π radian, and the diameter of the path is equal to the incircle diameter of the corresponding turning configuration. Then, the dynamic parameters are calculated by solving (18). In the constraint (1)–(4), the parameters that change for each turning mode are joint angles (θ_i) and incircle radius (R). This is shown in Table 4. The above steps are repeated for each configuration ($n = 4, 5, 6, 7, 8, 9, 10$) and corresponding parameters including thrust and joint torque requirements are calculated. The maxima and minima for the same are also noted. The simulation is carried out using MATLAB software. The simulation frame used is a square grid (X and Y range from −0.65 to 0.65 m). Since the vehicle's overall length is nearly 1.3 m, this gives the idea of reducing turning diameter with split hulls.

5 Results of the Analysis

Calculated values are shown in Table 4. As expected, the turning diameter goes on increasing with the turning mode number (n). Turning diameter crosses 1.3-m length when n becomes 10. Our configuration has to be limited to $n = 10$ to have a turning diameter smaller than body length (note that vehicle length is 1.28 m). Any value beyond that is not desirable as our ultimate goal is to bring the turning diameter well below the vehicle length. Another exciting trend is the variation of the axial thrust requirement. It increases with n up to Pentagonal orientation, but after that, it starts decreasing. The rise in force requirement is high when n is less than 5. Once it starts reducing after 5, the reduction rate decreases and slowly attains a steady value. This is because as the n increases, the turning path changes more into a straight line. Hence, the minimum thrust requirement will become nearly equal to the axial drag force in a straight-line path. This holds especially when n is very high ($n > 20$). So, the hexagon is a critical point for the thrust requirement. One has to go for a smaller thrust from an energy point of view. The values are also plotted in Figure 8. The variation of the thrust requirement is evident here. The maximum thrust that the surge thrusters can produce is 48 N. This is far higher than what is required as per the analysis. When it comes to joint torque requirements, it reduces gradually as n increases. Note that the torque requirement is very high for lower turning mode numbers ($n = 4, 5$). The difference in torque requirement is very high initially. Then it reduces slowly as n increases. This matches our previous assumption that rectangular ($n = 4$) configuration requires too much effort from the servo motors. Even at 0.4 m/s, it requires almost twice the torque amount as a hexagonal configuration (1.964 N·m vs 1.134 N·m). Based on the analysis, we have decided to go with a hexagonal configuration with all parameters at a moderate level. Though the force requirement is on the higher side than other modes, the difference is negligible compared to the vehicle's thrust capacity. Moreover, the turning diameter is lower (0.74 m), and most importantly, the joint torque is within the servo limit (1.14 N·m). Simultaneously, the thrust difference is negligible compared to thruster capacity, and

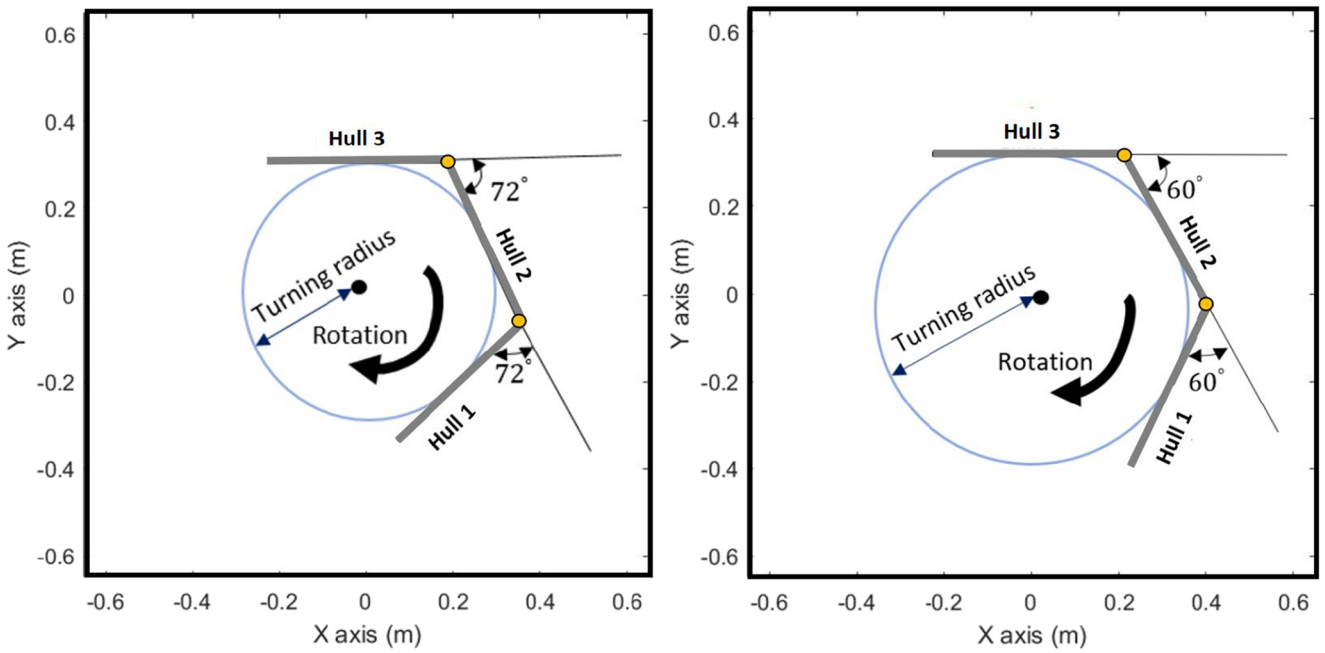

(a) Pentagonal ($n = 5$)

(b) Hexagonal ($n = 6$)

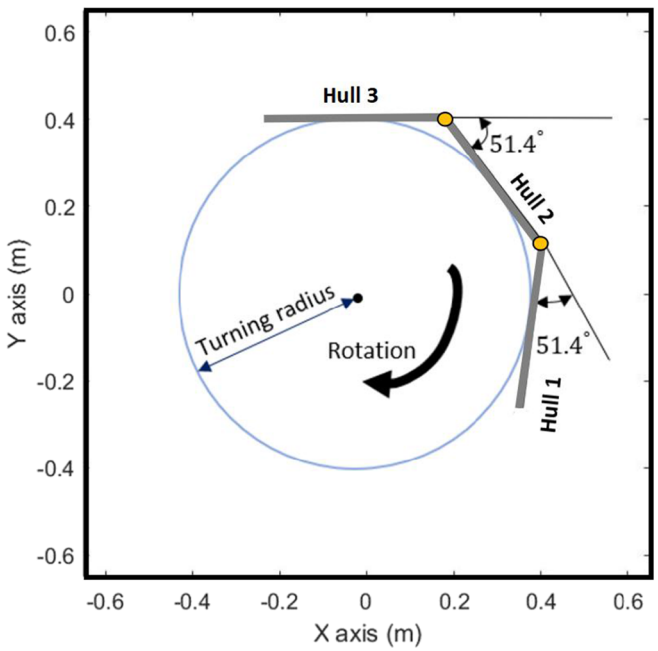

(c) Heptagonal ($n = 7$)

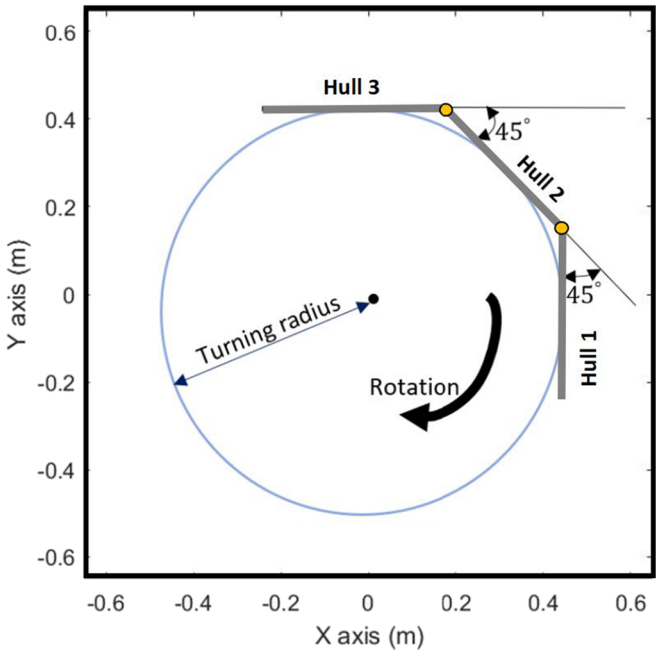

(d) Octagonal ($n = 8$)

Figure 7 Different configurations of the vehicle while taking a U-turn

the torque requirement is much lower than pentagonal and square modes. Hence, we conducted extensive studies on the hexagonal configuration. The simulation parameters in the case of turning in the hexagonal configuration are shown in Table 5, and the results for the same are given in the preceding sections. This includes the variation of linear velocity, linear acceleration, thrust, and torque requirement.

5.1 Velocity and Acceleration Analysis

The variations of X and Y components of velocity for each hull are shown in Figure 9a. Note that absolute velocity is always constant at 0.4 m/s (surge velocity). The velocity components change cyclically due to the hull's varying orientation with respect to the inertial frame. We assume that the turning diameter does not change with respect to

Table 4 Comparison of turning modes in terms of thrust, joint torque requirements and turning diameter

n	ϕ_{ij} (°)	$2R$ (m)	τ_{ij} (N·m)	T (N)
4	90	0.426	1.964	6.747
5	72	0.587	1.427	7.494
6	60	0.740	1.134	7.326
7	51.43	0.886	0.946	6.935
8	45	1.030	0.813	6.519
9	40	1.172	0.715	6.136
10	36	1.313	0.638	5.802
11	32.72	1.453	0.576	5.514
12	30	1.592	0.526	5.267

time. Hence, the angular velocity is constant (Choi and Choi 2015), and the angular acceleration is zero. The simulation is started by moving the hull three along $+Y$ direction at a speed of 0.4 m/s. So, velocity is purely Y directional for the same hull at $\beta = 0$. Slowly, X component gains its value. In the same way, all the hulls follow the same pattern with a phase shift. As the linear velocity and angular velocity are kept constant, tangential acceleration will be zero. But due to the rotational motion, centripetal acceleration will be present. It is resolved into both X and Y components of accelerations of the vehicle. This is shown in Figure 9b. The absolute value of the acceleration is 0.433 m/s^2. The variation of the components for all the hulls are shown in the same figure.

5.2 Thrust and Joint Torque requirements

The variation of axial thrust required during the revolution is shown in Figure 10a–b. Unlike velocity and acceleration analysis, the force values for the remaining hulls are not shown in the figure as the surge thrusters are fixed only on the front hull. Based on the calculation using Eqs. (16) and (18), the axial thrust's absolute value is found as 7.326 N, and its X and Y components vary with respect to the vehicle's orientation. As per the calculations given in Section 4.3, the joint torque requirement variation during the complete revolution is shown in Figure 10c. The torque on each joint remains constant at 1.134 N·m throughout the motion. This is expected as each hull's relative angular orientation does not change with respect to time and there is no unsteady force acting on the vehicle either. This is the torque required to hold the individual hulls to maintain the particular configuration while turning (hexagonal). This torque is an important factor as the capacity of the servo motor limits it. Any value higher than 1.14 N·m will severely damage the servo in our case. The effect of turning speed on the vehicle is analysed next.

Table 5 Theoretical parameters for hexagonal turning configuration

Parameter	Value
Linear speed (v)	0.4 m/s
Tangential acceleration (a)	0 m/s^2
Turning diameter ($2R$)	0.74 m
Angular speed (ω)	1.083 rad/s
Angular acceleration (α)	0 rad/s^2
Joint angles (ϕ_{12}, ϕ_{23})	60°

5.3 Effect of the Turning speed

All the above analyses were carried out at a speed of 0.4 m/s. However, the vehicle can surge even at 2 m/s along a straight path. We intend to check whether the vehicle can safely make a U-turn while it is surging at such speeds. Hence, we analysed the vehicle at different velocities of magnitude ranging from 0 m/s to 2 m/s. The results are plotted in Figure 11a and b. As expected, both thrust and torque are increasing with the increase in velocity in an exponential manner. The thrust requirement is 178 N to rotate the vehicle at a speed of 2 m/s. This is not possible as the two T100 thrusters combined can provide only up to a maximum of 48 N thrust. It is also found that the torque requirement for 2 m/s is 28.8 N·m which is very high compared to the capacity of the servo joints (1.14 N·m). Hence, the idea

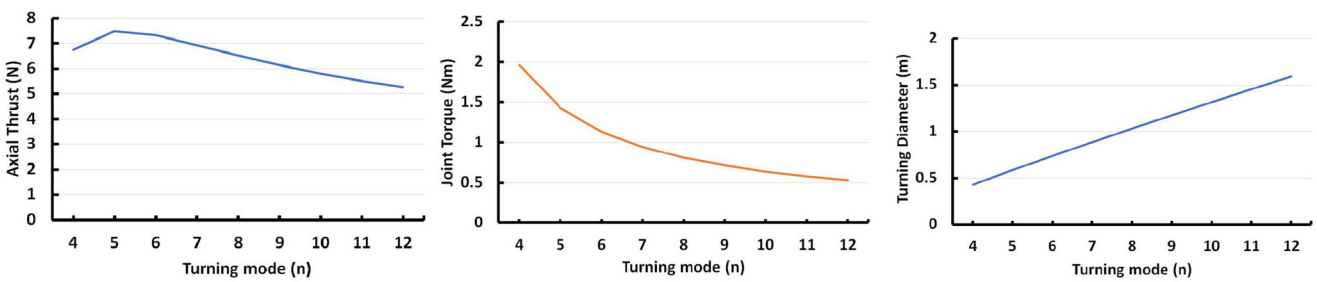

(a) Axial thrust required for turning (b) Joint Torque requirement (c) Turning diameter

Figure 8 Schematic diagram showing the effect of turning mode (n) on different parameters

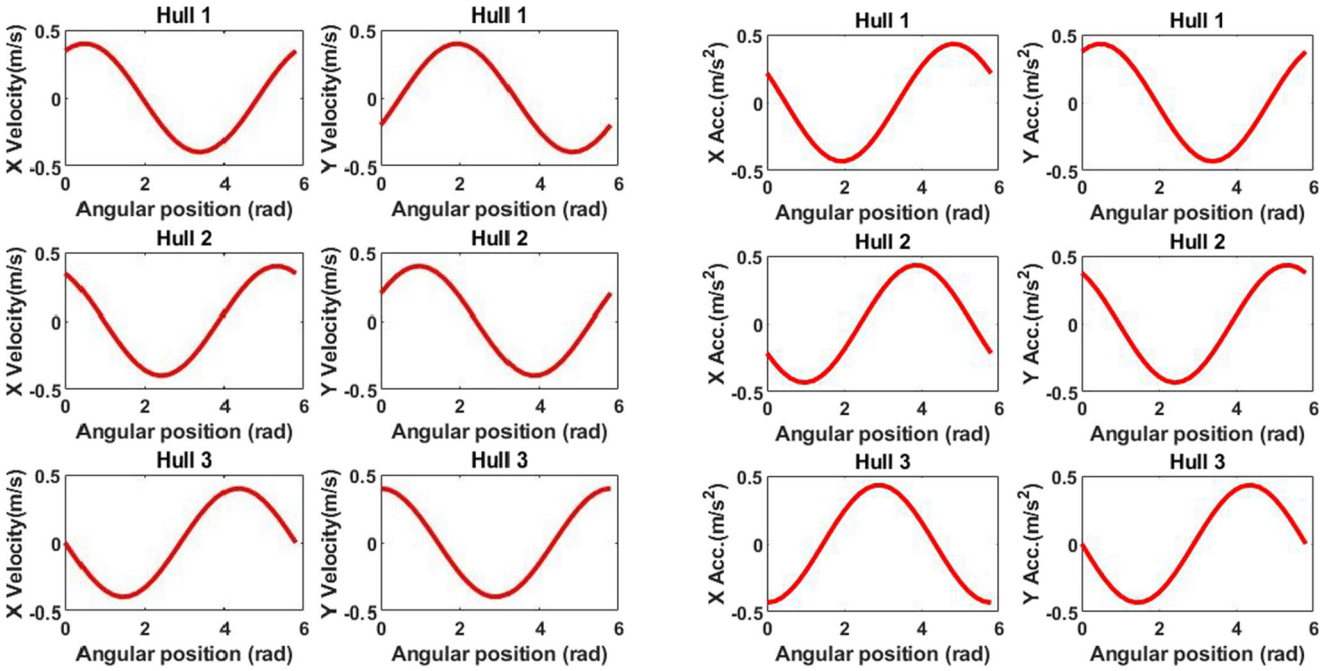

(a) Velocity (b) Acceleration

Figure 9 Variation of velocity and acceleration of each hull during rotation (Acc, Acceleration)

to conduct the turning motion at such a speed is not recommended. We will have to slow the vehicle down to make a safe turn. We also calculated the critical speed for turning. From Figure 11a and b, by keeping the torque limit as 1.14 N·m, the corresponding turning speed is 0.41 m/s. Note that the corresponding thrust requirement is 7.68 N, significantly less than the vehicle's thrust capacity.

6 Experimental Verification

The validity of theoretical modelling is verified using the experimental results. The vehicle is made to trace a circular path at different turning speeds starting from 0.1 m/s. The driving parameters (thrust and joint angles) are chosen according to the configuration and speed. Based on the results of critical speed analysis, the maximum turning speed is taken as 0.4 m/s. We chose the hexagonal configuration, and hence the joint angles are $\phi_{12} = 60°$ and $\phi_{23} = 60°$. Based on the analysis, the thrust and torque requirements are calculated using Eqs. (16), (18), (28), and (29). The thrusters we used are Bluerobotics T100, and the combined thrust and efficiency characteristics provided by the manufacturer (Robotics 2020) is shown in Fig. 11c. From Eq. 18, the total thrust requirement for 0.4 m/s is calculated as 7.326 N, and the corresponding thruster input signal is 1600 from the characteristic graph. Using these input values (T, ϕ_{ij}), the vehicle is operated at a constant depth of 0.12 m, and the corresponding turning diameter

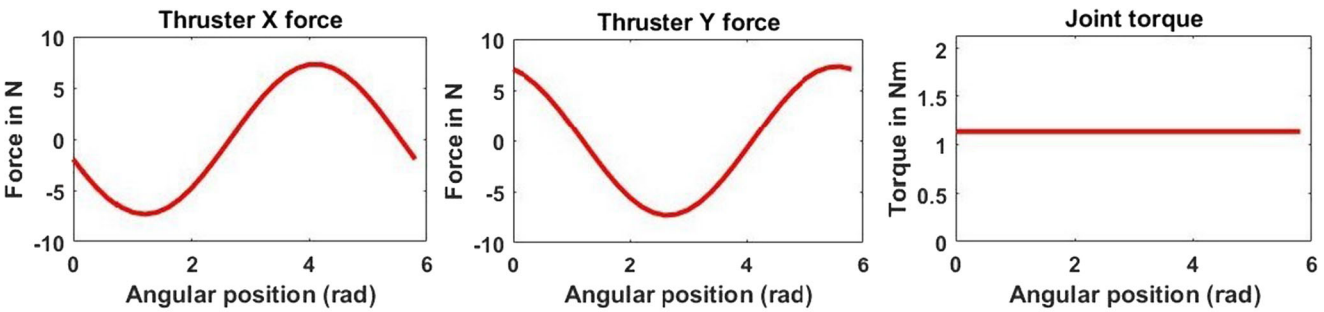

(a) X component of thrust (b) Y component of thrust (c) Joint Torque requirement

Figure 10 Variation of thrust and joint torque requirements during rotation

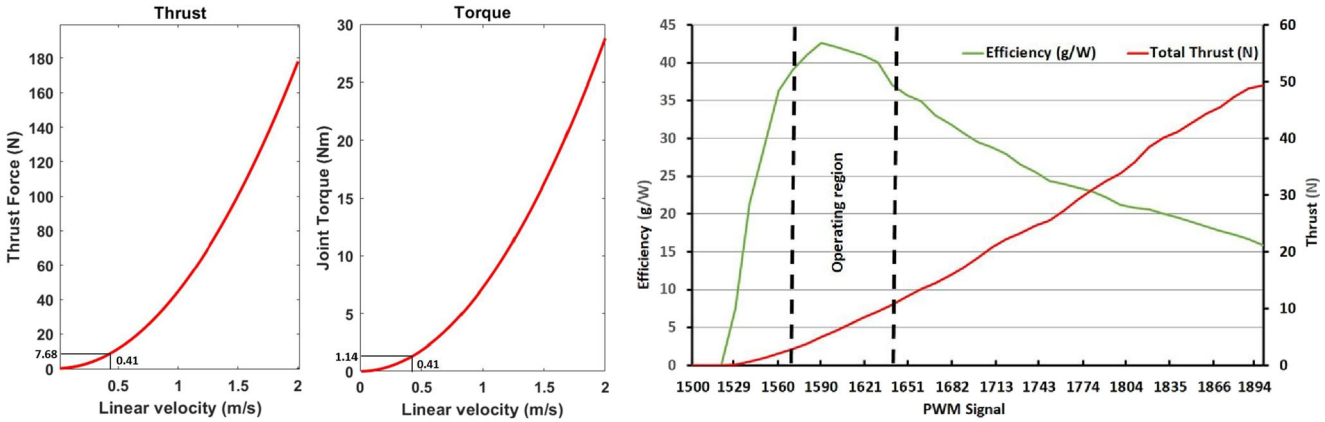

(a) Axial thrust requirement (b) joint torque requirement (c) Thrust characteristics and the operating region

Figure 11 Effect of turning speed on the axial thrust and joint torque requirements and the diagram showing the thrust characteristics of the vehicle

and speed are measured. To accurately measure the movements of the vehicle, underwater grid lines are used. This is shown in Figure 12a. The grid spacing used here is 0.7 m and is fixed at a depth of 1.5 m. They are fixed at this depth for easy turning diameter measurements and ensure the vehicle's smooth movement. Also, note the vehicle's relative dimensions (length of 1.28 m) with respect to grid size (0.7 m) from the same figure. The snapshots of the hexagonal configuration movements are shown in Figure 12b–c. It is recorded that in all the speeds, the vehicle aligns in hexagonal configuration properly and manages to take a turn with a diameter slightly higher than the theoretical value of 0.74 m. This error increases with the turning speed. This is shown in Table 6. This is because of the vehicle's slipping motion in the fluid medium due to inertial forces (Antonelli et al. 2016) that increases with speed. As the vehicle is neither pivoted to its centre of rotation nor having a sway thruster, this adverse effect cannot be avoided. Hence, this issue is common for all underwater vehicles. This points out another need for reducing the speed of the vehicle before taking a U-turn. But this error is negligible (<2%) when the turning speed is within the designed value of 0.4 m/s. The next step is the measurement of turning speed which is measured using a vertical camera setup. The snapshots of the movements at 0.4 m/s in the hexagonal configuration are shown in Figure 13a–e. It took 5.98 s to complete the rotational motion with a turning diameter of 0.75 m. This corresponds to a linear speed of 0.394 m/s. This value is slightly less than the theoretical speed of 0.4 m/s, and the corresponding error is 1.5%. This is because we ignored the action of thruster outlet flow on the other hulls in this analysis. This results in a slightly higher drag force compared to our calculation. But this effect is negligible at normal turning speeds (<0.5 m/s), and hence we continued the analysis with the same coefficients. The same procedure is repeated for 0.1–0.3 m/s as well, and the measured values are shown in Table 6. The torque requirement calculation holds as the servos easily handle the hulls in the required orientation even at 0.4 m/s. Because of the risk of damaging the servo motors, we did not operate the vehicle above that

(a) Vehicle and the grid lines (b) Vehicle with hulls rotated (c) Hexagonal turning mode

Figure 12 Photographs of M-Hull showing the relative size of vehicle with grid lines, the rotated form of hulls and the hexagonal turning mode

Table 6 Measured values and corresponding errors for Hexagonal configuration, Turning diameter=0.74 m

Velocity (m/s)	Thrust required (N)	Joint torque required (N·m)	Measured turning diameter (m)	Error in turning diameter (%)	Measured turning speed (m/s)	Error in turning speed (%)
0.1	0.637	0.072	0.74	0	0.099	1
0.2	2.029	0.288	0.74	0	0.198	1
0.3	4.290	0.648	0.75	1.4	0.296	1.33
0.4	7.326	1.131	0.75	1.4	0.394	1.5

speed. Note from Figure 11c that the thruster efficiency is maximum in the operating region corresponding to 0.2–0.5 m/s. Hence, it is decided to operate the vehicle at 0.4 m/s turning speed for future operations.

7 Conclusions and Future Works

We have discussed the development, modelling, and analysis of a split-hull AUV used to map water bodies. We

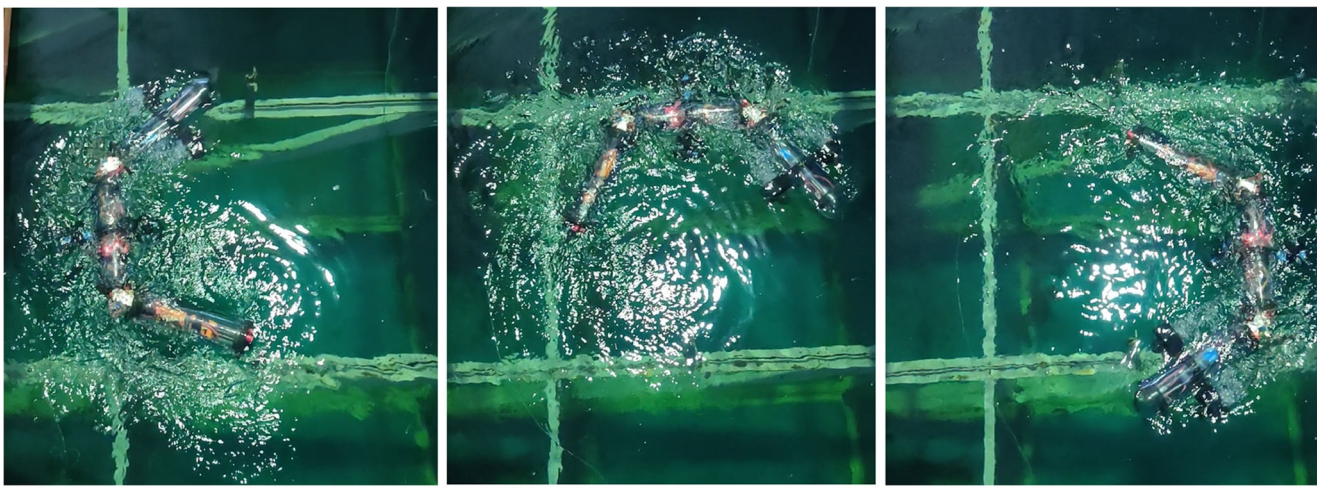

(a) t=0 s, $\beta = 0$ rad (b) t=1.49 s, $\beta = \pi/2$ rad (c) t=3 s, $\beta = \pi$ rad

(d) t= 4.48 s, $\beta = 3\pi/2$ rad (e) t= 5.98 s, $\beta = 2\pi$ rad

Figure 13 Photograph of M-Hull while turning at 0.4 m/s in hexagonal configuration at different instances

have analysed various turning modes and their influence on the performance of the vehicle. The split-hull design significantly reduces the turning diameter. For instance, the turning diameter achieved from the Hexagonal configuration is just 58% of the total length of the vehicle. It is a considerable improvement over conventional torpedo-shaped AUVs. Moreover, the better agility due to the thrusters over bio-inspired solutions makes it a better deal for extended operations. Simultaneously, the use of split-hulls with joint control system facilitates the flexibility of snake-like vehicles. Hence, this vehicle acts as an innovative hybrid solution between conventional torpedo-shaped vehicles and unconventional bio-inspired underwater vehicles. It leads to a new AUV class where agility and manoeuvrability come together without compromising the payload capacity. The influence of the split-hull design on the turning diameter and operating speed is studied, and the method followed here can be applied to any underwater vehicle with a split-hull design. We have also shown the merits and demerits of this design and realised that the turning speed is the critical parameter for safety and power consumption. As the analysis is conducted based on a few theoretical assumptions, the experimental values are slightly different. It is also noted that the higher the turning speed, the higher will be the error in speed and the vehicle's risk. But the modelling is reliable as the error values are below 2% even for the designed maximum turning speed of 0.4 m/s. We realised that servo joints are vulnerable to damage at higher turning speeds from the critical turning speed analysis. It is a demerit of split-hull designs due to which selection of a high-torque servo is essential. But as most AUVs slow down well below 0.4 m/s while taking a U-turn, this issue will not affect the performance of the vehicle in a practical scenario.

The plans include higher torque servo joints to overcome the limitation on the turning speed. Detailed modelling of the effect of surge thruster outflow on the other hulls and vehicle slipping effect at such operating speeds has to be carried out. We are also optimising the lateral thrust requirements and effects of water currents and waves on the multi-hull vehicle. Implementing a flexible cylindrical material over servo joints to reduce the drag force and make the vehicle more efficient is also being done.

Acknowledgements The authors would like to thank Rajesh K and Vishnu C from the Ocean Engineering department for their support during the experiments. Thanks to Murali S from the Mechanical Department for their efforts during the vehicle's fabrication. Special thanks to Sreehari V for the assistance during the development of the vehicle.

References

Abreu PC, Botelho J, Góis P, Ribeiro J (2016) The medusa class of autonomous marine vehicles and their role in eu projects. In: OCEANS 2016 - Shanghai, pp 1–10

Alvarez A, Caffaz A, Caiti A, Casalino G (2009) Fòlaga: a low-cost autonomous underwater vehicle combining glider and AUV capabilities. Ocean Eng 36(1):24–38. https://doi.org/10.1016/j.oceaneng.2008.08.014

Antonelli G (2014) Underwater robots. In: Springer Tracts in Advanced Robotics, vol 96. Springer Tracts in Advanced Robotics, pp 418–446

Antonelli G, Fossen TI, Yoerger DR (2016) Modeling and control of underwater robots. In: Springer Handbook of Robotics. Springer, pp 1285–1306

Betsch (2018) Computational dynamics Altenbach H, Öchsner A (eds), Springer, Berlin. https://doi.org/10.1007/978-3-662-53605-6_22-1

Chen W, Xia D, Liu J (2008) Modular design and realization of a torpedo-shape robot fish. In: Proceedings of 2008 IEEE International Conference on Mechatronics and Automation, ICMA 2008, Takamatsu, pp 125–130

Choi H-T, Choi J (2015) Requirements and design of highly accurate position control system for underwater visual inspection. In: OCEANS 2015 - Genova, pp 1–5. https://doi.org/10.1109/OCEANS-Genova.2015.7271568, http://ieeexplore.ieee.org/stamp.jsp?tp =&arnumber=7271568

Cox RG (1970) The motion of long slender bodies in a viscous fluid. Part 1. General theory. J Fluid Mech 44:791–810. https://doi.org/10.1017/S002211207000215X

Crespi AJA (2006) AmphiBot II : an amphibious snake robot that crawls and swims using a central pattern generator. Conference on Climbing and Walking Robots, London, pp 19–27

Eriksen CC, Osse TJ, Light RD, Wen T (2001) Seaglider: a long-range autonomous underwater vehicle for oceanographic research. IEEE J Ocean Eng 26(4):424–436. https://doi.org/10.1109/48.972073

German CR, Yoerger DR (2008) Hydrothermal exploration with the autonomous benthic explorer. Oceanograph Res Papers 55(2):203–219. https://doi.org/10.1016/j.dsr.2007.11.004, http://www.sciencedirect.com/science/article/pii/S0967063707002580

Gherairi O, Ben Hamed M (2017) Kinematic model of underwater vehicle. In: International Conference on Green Energy Conversion Systems (GECS). IEEE, Hammamet, pp 1–5. http://ieeexplore.ieee.org/document/8066245/

Gus'kova NY, Makhortykh GV, Shcheglova MG (1998) Inertia and drag of elliptic cylinders oscillating in a fluid. Fluid Dyn 33(1):91–95. UDC:532.582.3L013.2

Jagadeesh P, Murali K, Idichandy VG (2009) Experimental investigation of hydrodynamic force coefficients over AUV hull form. Ocean Eng 36(1):113–118. https://doi.org/10.1016/j.oceaneng.2008.11.008

Kato N, Ito Y, Kojima J (1994) Control performance of autonomous underwater vehicle "AQUA EXPLORER 1000" for inspection of underwater cables. Proceedings of OCEANS'94 , Brest, pp 135–140. https://doi.org/10.1109/OCEANS.1994.363845, http://ieeexplore.ieee.org/lpdocs/epic03/wrapper.htm?arnumber=363845%5Cn http://ieeexplore.ieee.org/document/363845/

Kelasidi E, Pettersen KY (2015) Energy efficiency of underwater robots. 10th IFAC Conference on Manoeuvring and Control of Marine Craft, Copenhagen, Denmark 28(16):152–159. https://doi.org/10.1016/j.ifacol.2015.10.273

Kelasidi E, Pettersen KY, Liljeback P (2016) Locomotion efficiency of underwater snake robots with thrusters. SSRR 2016 - International Symposium on Safety, Security and Rescue Robotics, Lausanne, pp 174–181. https://doi.org/10.1109/SSRR.2016.7784295

Kelasidi E (2015) Modeling, control and energy efficiency of underwater snake robots. Ph.D thesis, Norwegian University of Science and Technology (NTNU),Trondheim, Norway

Khalil W, Gallot G (2007) Dynamic modeling and simulation of a 3-D serial eel-like robot. IEEE Trans Syst Man Cybern Part C (Appl

Rev) 37(6):1259–1268. https://doi.org/10.1109/TSMCC.2007.905831

Kumar VS, Rajagopal P (2019) Development and analysis of an autonomous underwater inspection vehicle with enhanced maneuverability. In: OCEANS 2019 - Marseille, France, pp 1–8

Kunz C, Murphy C, Singh (2009) Toward extraplanetary under-ice exploration: Robotic steps in the Arctic. J Field Robot 26(4):411–429. https://doi.org/10.1002/rob.20288

Liljeback P, Stavdahl O (2014) Mamba - A waterproof snake robot with tactile sensing. In: IEEE International Conference on Intelligent Robots and Systems, Chicago, pp 294–301

Liljeback P, Mills R (2017) Eelume: a flexible and subsea resident IMR vehicle. OCEANS 2017, Aberdeen, pp 1–4. https://doi.org/10.1109/OCEANSE.2017.8084826

Lin X (2011) Development of a spherical underwater robot. In: 2011 IEEE/ICME International Conference on Complex Medical Engineering, CME 2011, Heilongjiang, pp 662–665. https://doi.org/10.1109/ICCME.2011.5876823

Madhan R, Desa E, Prabhudesai S (2006) Mechanical design and development aspects of a small AUV - Maya. In: 7th IFAC Conference on Manoeuvring and Control of Marine Craft, Lisbon, pp 1–6. http://drs.nio.org/drs/handle/2264/702

Morison JR, Johnson JW, Schaaf SA (1950) The force exerted by surface waves on piles. J Pet Technol 2(5):149–154. https://doi.org/10.2118/950149-G

Newman JNJN, Grue J (1977) Marine hydrodynamics. The Massachusetts Institute of Technology (MIT) Press Cambridge, UK, pp 426. https://mitpress.mit.edu/books/marine-hydrodynamics-40th-anniversary-edition

Prestero T (2001) Verification of a six-degree of freedom simulation model for the REMUS100 AUV. MS Thesis, Massachusetts Institute of Technology, Cambridge, pp vol 1

Punning A, Anton M (2004) A biologically inspired ray-like underwater robot with electroactive polymer pectoral fins. International Conference on Mechatronics and Robotics, Istanbul. https://doi.org/10.1080/19475411.2012.686458

Robotics B (2020) Blue robotics t100. https://www.bluerobotics.com/store/thrusters/t100thruster. [Accessed on 19-06-2020]

Rollinson D (2014) Control and design of snake robots. Ph.D thesis, School of Computer Science Carnegie Mellon University Pittsburgh, PA. http://repository.cmu.edu/dissertations/427

Shabana AA (2013) Dynamics of multibody systems. In: Dynamics of Multibody Systems. 1st edn. Cambridge University Press, Cambridge, England, pp 72–89

Sverdrup-Thygeson J, Kelasidi E (2018) The underwater swimming manipulator - a bioinspired solution for subsea operations. IEEE J Ocean Eng 43(2):402–417. https://doi.org/10.1109/JOE.2017.2768108

Tamura K, Aoki T, Nakamura T (2000) The development of the auv-urashima. In: OCEANS 2000 MTS/IEEE Conference, Providence, pp vol 1, pp 139–146

Venugopal V, Varyani KS, Westlake PC (2009) Drag and inertia coefficients for horizontally submerged rectangular cylinders in waves and currents. J Eng Maritime Environ 223(1):121–136. https://doi.org/10.1243/14750902JEME124

Wang S, Wang Y, Wei Q, Tan M, Yu J (2017) A bio-inspired robot with undulatory fins and its control methods. IEEE/ASME Trans Mechatron 22(1):206–216. https://doi.org/10.1109/TMECH.2016.2622761

Wiens AJ, Nahon M (2012) Optimally efficient swimming in hyper-redundant mechanisms: control, design, and energy recovery. Bioinspir Biom 7(4):046016. https://doi.org/10.1088/1748-3182/7/4/046016

Yu J, Wang L (2007) Geometric optimization of relative link lengths for biomimetic robotic fish. IEEE Trans Robot 23(2):382–386. https://doi.org/10.1109/TRO.2007.892221

Zhang C, Hedrick TL, Mittal R (2015) Centripetal acceleration reaction: an effective and robust mechanism for flapping flight in insects. PloS one 10(8):e0132093. https://doi.org/10.1371/journal.pone.0132093

Zuo Z, Wang Z (2008) Serpentine locomotion of a snake-like robot in water environment. In: 2008 IEEE International Conference on Robotics and Biomimetics, ROBIO, Bangkok, pp 25–30